NANO · MICRO small
www.small-journal.com

# High-Energy-Density Cathode Achieved via the Activation of a Three-Electron Reaction in Sodium Manganese Vanadium Phosphate for Sodium-Ion Batteries

*Yuxiang Chen, Qingping Li, Peng Wang, Xiangyue Liao, Ji Chen, Xiaoqin Zhang, Qiaoji Zheng,* Dunmin Lin,* and Kwok-ho Lam**

**Sodium superionic conductor (NASICON)-type $Na_3V_2(PO_4)_3$ has attracted considerable interest owing to its stable three-dimensional framework and high operating voltage; however, it suffers from a low-energy density due to the poor intrinsic electronic conductivity and limited redox couples. Herein, the partial substitution of $Mn^{3+}$ for $V^{3+}$ in $Na_3V_2(PO_4)_3$ is proposed to activate $V^{4+}/V^{5+}$ redox couple for boosting energy density of the cathodes ($Na_3V_{2-x}Mn_x(PO_4)_3$). With the introduction of $Mn^{3+}$ into $Na_3V_2(PO_4)_3$, the band gap is significantly reduced by 1.406 eV and thus the electronic conductivity is greatly enhanced. The successive conversions of four stable oxidation states ($V^{2+}/V^{3+}$, $V^{3+}/V^{4+}$, and $V^{4+}/V^{5+}$) are also successfully achieved in the voltage window of 1.4–4.0 V, corresponding to three electrons involved in the reversible reaction. Consequently, the cathode with $x = 0.5$ exhibits a high reversible discharge capacity of 170.9 mAh $g^{-1}$ at 0.5 C with an ultrahigh energy density of 577 Wh $kg^{-1}$. Ex-situ x-ray diffraction (XRD) analysis reveals that the sodium-storage mechanism for Mn-doped $Na_3V_2(PO_4)_3$ consists of single-phase and bi-phase reactions. This work deepens the understanding of the activation of reversible three-electron reaction in NASICON-structured polyanionic phosphates and provides a feasible strategy to develop high-energy-density cathodes for sodium-ion batteries.**

## 1. Introduction

As known, lithium-ion batteries (LIBs) are the most commercially successful electrochemical energy-storage devices over the past 30 years owing to their high-energy density and long cycle life.[1–3] However, the sustainable application of LIBs is greatly hindered by the low abundance and geographically uneven distribution of lithium resources in the earth's crust.[4–6] Recently, as one of the promising alternative candidates for LIBs, sodium-ion batteries (SIBs) have been widely favored due to their low cost and similar physicochemical characteristics to LIBs.[7–10] However, the limited energy density of SIBs hinders the commercialization. Thus, competitive cathodes with high cost-effectiveness and excellent electrochemical performance are highly desired to develop so as to enhance the market values of SIBs.[11,12]

In recent years, several cathode families for SIBs have been reported, including layered metal oxides,[12–14] Prussian blue homologues,[15] and polyanionic compounds.[16–18] Among them, $Na_3V_2(PO_4)_3$ (NVP) has received increasing attention as one of the best choices for the cathodes of SIBs, which is attributed to its robust three-dimensional frame for $Na^+$ transportation, small volume change during $Na^+$ extraction/insertion, and high redox potential induced by the powerful inductive effect between transition metal and phosphates.[19–21] However, the low electronic conductivity of pure NVP leads to poor rate performance and inferior cycling stability, and thus several modification strategies have been developed to address the aforementioned issues, as shown in **Figure 1**a.[19,22–26] Among the strategies, element doping has attracted considerable attention due to its strong ability to intrinsically improve the electrochemical properties of NVP-based materials, especially the doping of V-site (Figure 1b).[11,27] Recently, diverse NVP-based cathodes have been developed by partially substituting $V^{3+}$ at V sites by transition metal ions based on the redox turnability of V element,[28,29] such as Mo-doped $Na_3V_2(PO_4)_3$@C,[30] $Na_3VAl_{0.2}Cr_{0.2}Fe_{0.2}In_{0.2}Ga_{0.2}(PO_4)_3$,[31] $Na_4V_{0.8}Al_{0.2}Mn(PO_4)_3$,[32] $Na_{3.9}Mn_{0.95}Zr_{0.05}V(PO_4)_3$/C,[33] $Na_3V_{1.6}Cr_{0.4}(PO_4)_3$,[34] and

Y. Chen, Q. Li, P. Wang, X. Liao, J. Chen, X. Zhang, Q. Zheng, D. Lin
College of Chemistry and Materials Science
Sichuan Normal University
Chengdu 610066, P. R. China
E-mail: joyce@sicnu.edu.cn; ddmd222@sicnu.edu.cn
K.-ho Lam
Centre for Medical and Industrial Ultrasonics
James Watt School of Engineering
University of Glasgow
Glasgow, G12 8QQ Scotland, United Kingdom
E-mail: kwokho.lam@glasgow.ac.uk

The ORCID identification number(s) for the author(s) of this article can be found under https://doi.org/10.1002/smll.202304002



**DOI: 10.1002/smll.202304002**

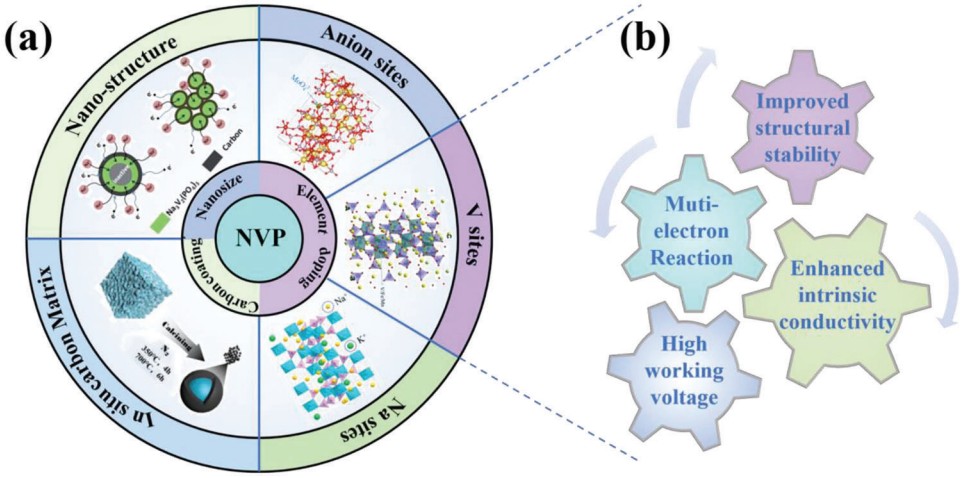


**Figure 1.** a) Schematic diagram of modification strategies of NVP.[19,22–26] b) Advantages of element doping at V sites in NVP.[11,27]

$Na_{3.75}V_{1.25}Mn_{0.75}(PO_4)_3$.[35] However, most of NVP-based materials generally only involve 1–2 electrons transferred per chemical formula unit based on the redox couple of $V^{3+}/V^{4+}$ during electrochemical reactions within the voltage range of 2.3–4.5 V, delivering the inferior capacity and unsatisfactory energy density.[36,37] Recently, it has been found that the key of increasing the energy density of cathodes is to involve more than two electrons in the electrochemical processes by making full use of the three redox couples of vanadium elements ($V^{2+}/V^{3+}$, $V^{3+}/V^{4+}$, and $V^{4+}/V^{5+}$). For example, Zhao et al. pioneered that the appropriate doping of $Cr^{3+}$ in the NVP could activate $V^{4+}/V^{5+}$ to successfully achieve a reversible three-electron reaction, which presents the excellent capacity of 150 mAh $g^{-1}$ at 30 mA $g^{-1}$ within 1.0–4.4 V;[20] further studies on Cr-doped NVP by Chen et al. and Zhang et al. found that the band gaps of $Na_3V_{1.5}Cr_{0.5}(PO_4)_3$ are reduced due to the 3d orbitals of Cr dopant, thus improving the electron conductivity; and the ionic conductivity in the local structure is improved due to the fact that Cr [Ar]$3d^5 4s^1$ has one more valence electron than V [Ar]$3d^3 4s^2$, favoring the electrochemical activity and thus inducing the excellent specific capacity and energy density.[11,16] Since then, similar studies involving three-electron chemistry have been reported as follows: the doping of $Al^{3+}$ into the NVP ($Na_3V_{1.5}Al_{0.5}(PO_4)_3$) activates the $V^{4+}/V^{5+}$ redox couple at 3.9 V and thus effectively achieves the capacity of 163 mAh $g^{-1}$ at 0.1 C;[27] and the introduction of $Ti^{4+}$ or $Fe^{3+}$ induces the similar three-electron effect in NASICON-type phosphates, giving significantly enhanced specific capacity and energy density (($Na_2TiV(PO_4)_3$: 187 mAh $g^{-1}$ at 0.1 C in 1.5–4.5 V;[38] $Na_{3.41}£_{0.59}FeV(PO_4)_3$ (£: Na vacancy): 170 mAh $g^{-1}$ at 0.5 C in 1.5–4.4 V[39]). Moreover, inexpensive manganese has also been frequently introduced into the NASICON-type polyanion phosphates.[7,40] For example, Klee et al. synthesized $Na_3V_{1.7}Mn_{0.3}(PO_4)_3$ via a sol–gel method, presenting capacities of 104 mAh $g^{-1}$ at 0.5 C and 92 mAh $g^{-1}$ at 2 C in the voltage range of 2.0–4.3 V based on $V^{3+}/V^{4+}$ couple with two electrons involved in the reaction;[41] Zhang et al. prepared $Na_{3.5}V_{1.5}Mn_{0.5}(PO_4)_3$ nanoparticles with the doping of $Mn^{2+}$ and found that the couple of $V^{4+}/V^{5+}$ at 3.9 V is successfully activated after doped with $Mn^{2+}$, demonstrating a capacity of 100.2 mAh $g^{-1}$ at 1 C between 2.5 and 4.1 V.[42] However, there are few reports on the multielectron reaction in NASICON-type polyanion phosphates induced by the doping of $Mn^{3+}$.

Herein, the doping of $Mn^{3+}$ into the $Na_3V_2(PO_4)_3$ is performed to activate the $V^{4+}/V^{5+}$ redox for boosting the $Na^+$ storage in the material ($Na_3V_{2-x}Mn_x(PO_4)_3$). After the introduction of $Mn^{3+}$ in the $Na_3V_2(PO_4)_3$, the band gap is significantly reduced for enhancing the intrinsic electronic conductivity and simultaneously activating high-potential $V^{4+}/V^{5+}$ redox couple successfully. As a result, the $Na_3V_{1.5}Mn_{0.5}(PO_4)_3$ possesses a high reversible discharge capacity of 170.9 mAh $g^{-1}$ at 0.5 C in the voltage window of 1.4–4.0 V with an ultrahigh energy density of 577 Wh $kg^{-1}$. What is more, an ex-situ analysis demonstrates the coexistence of two sodium-storage mechanisms of single-phase and bi-phase reactions.

## 2. Result and Discussion

The NASICON-type $Na_3V_{2-x}Mn_x(PO_4)_3$ cathodes [NVP-Mn($x$), $x$ = 0, 0.1, 0.3, 0.5, 0.7] are prepared by an ordinary high-temperature solid-state reaction. The Supporting Information section provides a comprehensive overview of all the experimental details. The crystal structures of the NVP-Mn($x$) are shown in **Figure 2**. All samples possess high crystallinity that can be associated with the rhombohedral NASICON structures with a space group of R-3c (Figure 2a). However, in the Mn-rich phosphates with $x$ = 0.5 and 0.7, tiny impurity peaks assigned to $Na_4Mn_3P_4O_{15}$ species are detected in the 2$\theta$ range of 20–35°. Specifically, the heteropeaks of the NVP-Mn(0.5) are so weak that its Rietveld refinement can be carried out smoothly (Figure 2e). As shown in Table S1 (Supporting Information, ICP-OES result), the actual composition of the NVP-Mn(0.5) is close to the stoichiometric ratio of the material. Figure 2a,b shows that all the diffraction peaks successively shift toward lower angles with $x$ increasing, illustrating the successful integration of $Mn^{3+}$ into the NASICON frame, leading to the lattice expansion due to $Mn^{3+}$ (0.785 Å) being larger than $V^{3+}$ (0.78 Å) and thus favoring $Na^+$ diffusion.[41] The XRD Rietveld refinements of the

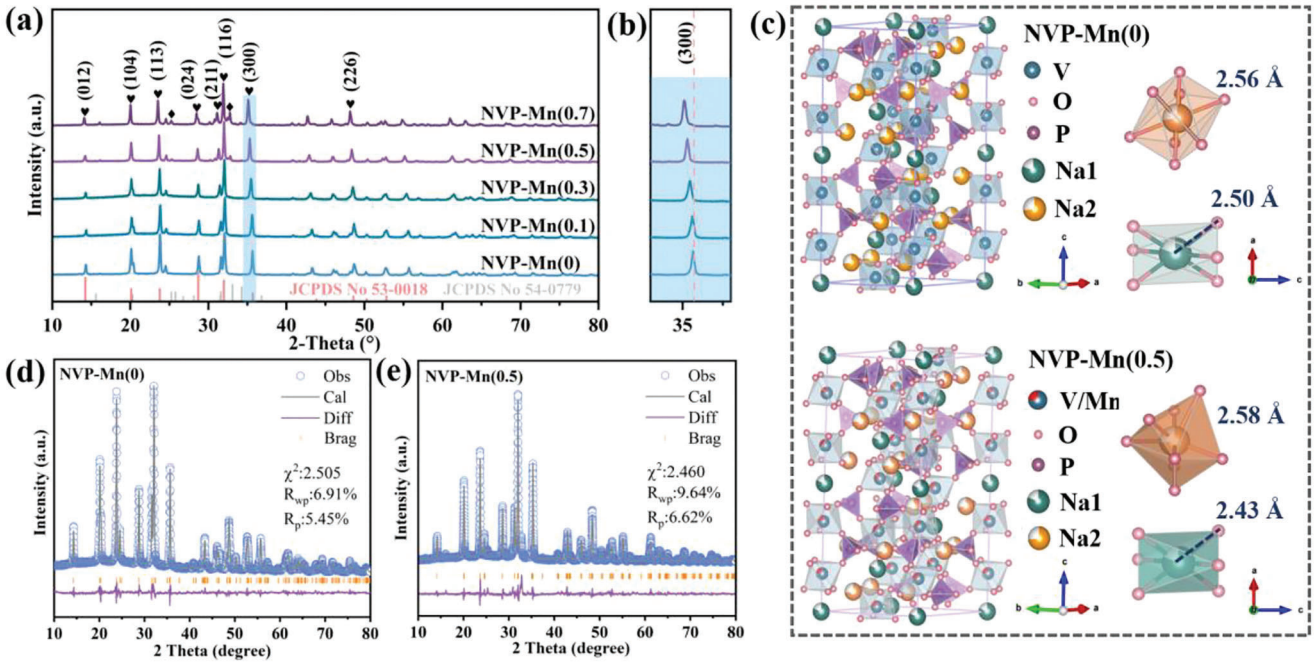


**Figure 2.** a,b) XRD patterns of NVP-Mn(*x*). c) Crystal structures of NVP-Mn(0) and NVP-Mn(0.5). Rietveld refinements for: d) NVP-Mn(0)) and e) NVP-Mn(0.5).

materials with $x = 0$ and 0.5 are carried out and the results are shown in Figure 2c–e and Tables S2–S3 (Supporting Information). The NVP-Mn(0) and NVP-Mn(0.5) materials possess the typical rhombohedral NASICON structure with R-3c space group[23] with $\chi^2$ below acceptable values ($R_{wp}$ = 6.91%/Rp = 5.45%/$\chi^2$ = 2.505 for the NVP-Mn(0); $R_{wp}$ = 9.64/Rp = 6.62%/$\chi^2$ = 2.460 for the NVP-Mn(0.5)). As shown in Tables S2 and S3 (Supporting Information), 25% of the V atoms is replaced by Mn, which is consistent with the designed NVP-Mn(0.5). The V atoms occupy the same sites as Mn atoms in [$MO_6$] (M = V, Mn) octahedral (Figure 2c). The [$VO_6$]/[$MnO_6$] octahedra is connected to [$PO_4$] tetrahedra by oxygen atoms to construct the basic "lantern" units [$Mn_{0.5}V_{1.5}(PO_4)_3$], providing the ion channels for rapid de/insertion of $Na^+$, while the $Na^+$ occupy two independent sites (6b, 18e) with Na1 located in the six-fold coordination oxygen at 6b and Na2 located in the eight-fold coordination oxygen at 18e.[43] In general, Na1 stabilizes the frame structure, while Na2 is more likely to be de/inserted during charging and discharging.[19] In our case, compared with the NVP-Mn(0), the NVP-Mn(0.5) has a shortened Na1-O bond and an elongated Na2-O bond (Table S2, Supporting Information), which is beneficial for the $Na^+$ diffusion.[44]

The carbon contents of the NVP-Mn(0) and NVP-Mn(0.5) are analyzed by CHNS elemental analysis and the result is shown in Table S4 (Supporting Information). It can be seen that the two materials possess almost the same carbon content (≈11%). The Raman spectra in **Figure 3**a reveal two similar characteristic carbon peaks for the NVP-Mn(0) and NVP-Mn(0.5) at 1342 and 1588 $cm^{-1}$, respectively, matching disordered (D band) and graphitized (G band) carbons, separately. Moreover, the $I_D/I_G$ values of the NVP-Mn(0) and NVP-Mn(0.5) are essentially equal (≈0.99 < 1), showing a partially graphitized carbon frame and thus suggesting good electrical conductivity for both materials.[44] The Survey XPS spectra (Figure S1, Supporting Information) of the NVP-Mn(0) and NVP-Mn(0.5) reveal similar elements of Na, V, P, O, and C, except for NVP-Mn(0.5) containing Mn. From Figure 3b, the C 1s spectra present three similar conductive carbons with distinct peaks, consistent with C–C (284.8 eV), C–O (286.3 eV), and O–C=O (288.7 eV) bonds, respectively. As shown in Figure 3c, for the V 2p of the NVP-Mn(0) and NVP-Mn(0.5), the two spin orbital peaks observed at 517.3/517 and 524.2/523.6 eV belong to trivalent $V^{3+}$, attributing to V $2p_{3/2}$ and V $2p_{1/2,}$ respectively; however, the peaks for the NVP-Mn(0.5) are finely shifted toward a lower binding energy compared with the NVP-Mn(0), declaring the increasing electron density at V sites after the doping of Mn ions[45] and thus leading to an increased electron transfer rate. In Figure 3d, for the NVP-Mn(0.5), the XPS spectrum of Mn 2p indicates two signal peaks situated at 653.7 and 641.9 eV, respectively, which correspond to trivalent $Mn^{3+}$ and are allocated to the orbitals of Mn $2p_{3/2}$ and $2p_{1/2}$.[23,46] The morphology and microstructure of the NVP-Mn(0.5) are presented in Figure 3e–i. From Figure 3e, the NVP-Mn(0.5) is comprised of inconsistent nanoparticles with unform size, but the size of the NVP-Mn(0) is extremely uneven with severe agglomeration of nanoparticles with irregular grains (Figure S2, Supporting Information). The uniform elemental distributions are detected in the NVP-Mn(0) and NVP-Mn(0.5) (Figures S3–S4, Supporting Information). The TEM picture (Figure 3f) of the NVP-Mn(0.5) presents that a complete carbon matrix is formed, which has a three-dimensional conductive network composed of a complete and continuous carbon frame, improving the overall conductivity of the cathode material.[44,47] From Figure 3g, the outer layer of the NVP-Mn(0.5) particles is coated with the ≈2.5 nm-thick carbon, and the lattice fringe with the spacing of 0.432 nm is

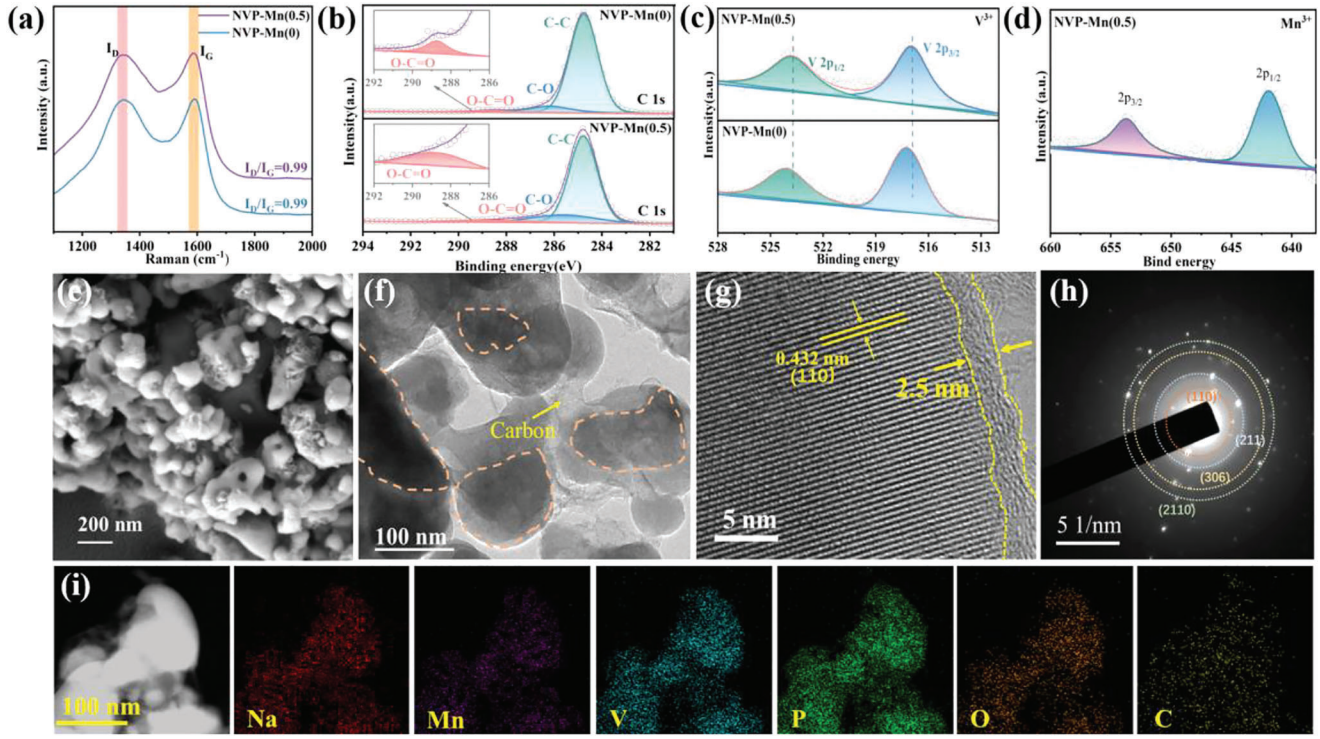


**Figure 3.** a) Raman spectra, b) XPS spectra of C 1s, and c) XPS spectra of V 2p for NVP-Mn(0) and NVP-Mn(0.5). d) XPS spectrum of Mn 2p, e) SEM image, f) TEM image, g) HRTEM image, h) SAED image, and i) EDS mapping images of NVP-Mn(0.5).

detected in the material, attributing to the (110) plane of the NASICON structure. The SAED image (Figure 3h) verifies the polycrystallinity of the NVP-Mn(0.5), while the corresponding elemental mapping images show that Na, Mn, V, P, O, and C are uniformly distributed in the NVP-Mn(0.5) (Figure 3i) and the content of elements is basically in line with the stoichiometric ratio of the material (Figure S5 and Table S5, Supporting Information).

The electrochemical behaviors of the NVP-Mn($x$) electrodes are evaluated in 2032-type coin cells. The cycling stabilities of the NVP-Mn($x$) electrodes at 1 C within 1.4–4.0 V are displayed in **Figure 4**a and Figure S6 (Supporting Information). Among the cathodes, the NVP-Mn(0.5) possesses the best specific capacity of 110.1 mAh g$^{-1}$ after 100 cycles, while the NVP-Mn(0), NVP-Mn(0.1), NVP-Mn(0.3), and NVP-Mn(0.7) only deliver inferior capacities of 53.3, 29.3, 83.7, and 74.0 mAh g$^{-1}$ after 100 cycles, respectively. From the corresponding GCD curves (Figure S7, Supporting Information), the polarization of NVP-Mn(0.5) is the weakest among four cathodes and thus the cathode with $x = 0.5$ would possess the best reversibility and cycle life.[48] Moreover, the NVP-Mn(0.5) could reliably cycle 300 times at 5 C, while the capacity of the NVP-Mn(0) decreases rapidly (Figure S8, Supporting Information). Figure 4b,c shows the charge/discharge curves of the NVP-Mn(0) and NVP-Mn(0.5) in the first ten cycles at 1 C. Compared with those of the NVP-Mn(0), the curves of the NVP-Mn(0.5) show much better overlap. In addition, the NVP-Mn(0.5) presents three distinct pairs of voltage plateaus, matching well with the reversible redox couples of $V^{2+/3+}$ (1.6 V), $V^{3+/4+}/Mn^{2+/3+}$(3.4 V), and $V^{4+/5+}$ (3.9 V),[6,11,16,27], respectively. Due to the close conversion voltage of $V^{3+}/V^{4+}$ and $Mn^{2+}/Mn^{3+}$, only a single voltage plateau is displayed in the NVP-Mn(0.5). Clearly, compared with the NVP-Mn(0), the additional voltage platform consistent with the $V^{4+/5+}$ redox couple is detected at 3.9 V in the NVP-Mn(0.5), leading to greater advantage in terms of energy density. As illustrated in Figure 4d, the first discharge capacity provided by the NVP-Mn(0.5) at 0.5 C is up to 170.9 mAh g$^{-1}$, proving that the three-electron redox reaction is achieved completely after the doping of $Mn^{3+}$.[27] The outstanding reversible capacities of 155.5, 145.4, 132.4, 114.4, 96.0, 85.5, and 79.4 mAh g$^{-1}$ are delivered in the NVP-Mn(0.5) at the rates of 1 C, 2 C, 3 C, 5 C, 7 C, 9 C, and 10 C, respectively. When the rate is back to 0.5 C, the capacity is returned to 156.2 mAh g$^{-1}$ and then the high capacity of 141.5 mAh g$^{-1}$ is maintained after 100 cycles, suggesting much better rate performance than the NVP-Mn(0). The galvanostatic charge–discharge (GCD) curves of the NVP-Mn(0) and NVP-Mn(0.5) are shown in Figure 4e, showing that the electrochemical polarization of the NVP-Mn(0.5) is subdued, demonstrating the superior rate performance compared with the NVP-Mn(0).[38] From Figure 4f and Figure S9 (Supporting Information), the dQ/dV plot obtained from the data in Figure 4e highlights three pairs of sharp oxidation/reduction peaks, attributing to the redox couples of $V^{2+/3+}$, $V^{3+/4+}/Mn^{2+/3+}$, and $V^{4+/5+}$, respectively, suggesting the continuous transformations of $Na_4V_{1.5}Mn_{0.5}(PO_4)_3 \leftrightarrow Na_3V_{1.5}Mn_{0.5}(PO_4)_3 \leftrightarrow Na_{1.25}V_{1.5}Mn_{0.5}(PO_4)_3 \leftrightarrow NaV_{1.5}Mn_{0.5}(PO_4)_3$. On the other hand, the dQ/dV plot of the NVP-Mn(0) only exhibits two pairs of oxidation/reduction peaks, in agreement with the redox couples of $V^{2+}/V^{3+}$ and $V^{3+}/V^{4+}$, respectively. From Figure 4g and Table S6 (Supporting Information), the operating voltage and energy density of the NVP-Mn(0.5) are ≈3.38 V and ≈577 Wh kg$^{-1}$ at 0.5 C,

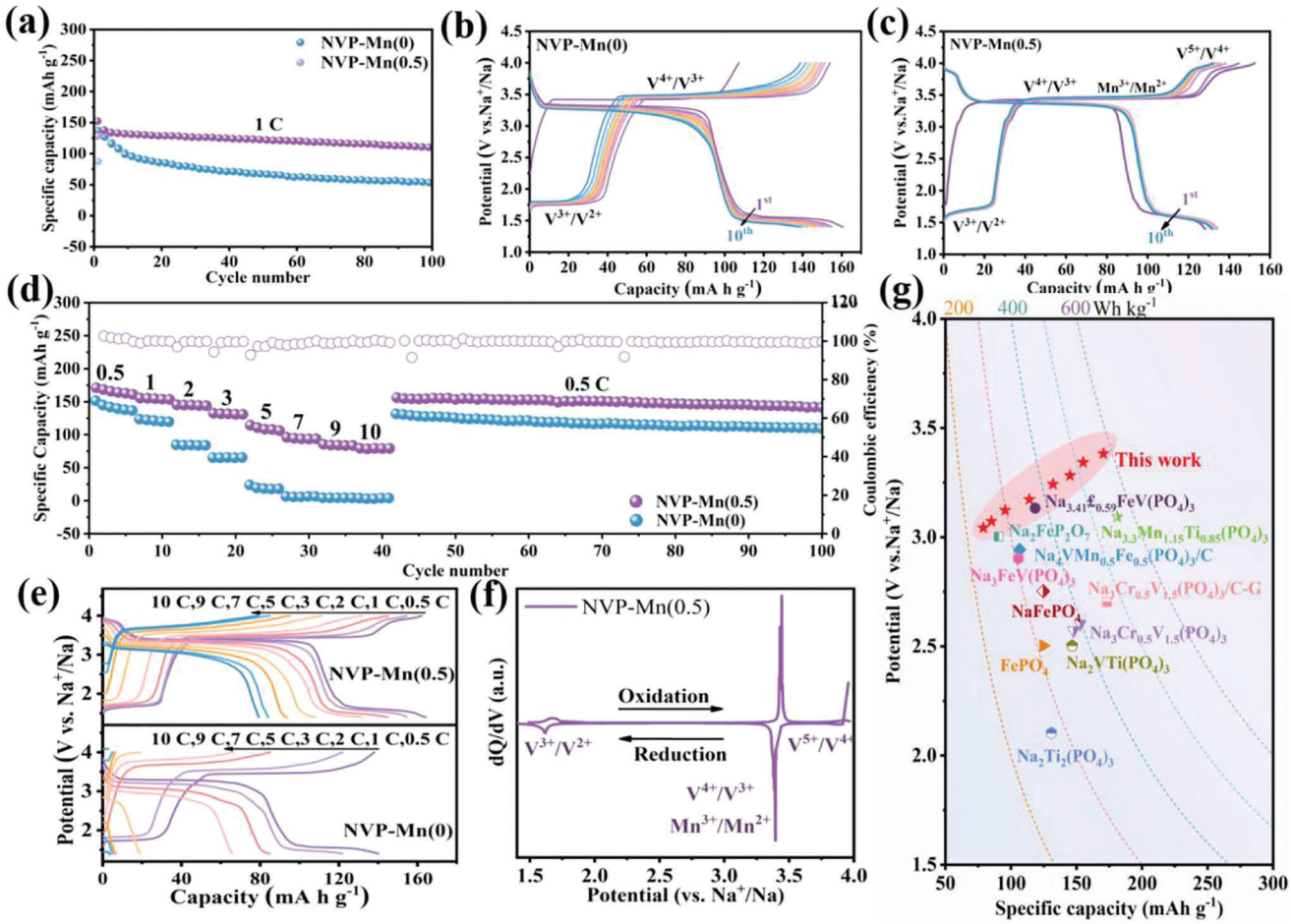


**Figure 4.** Electrochemical properties of NVP-Mn(0)and NVP-Mn(0.5). a) Cycling performance at 1 C. b,c) Charge/discharge curves for the initial ten cycles. d) Rate performance and e) corresponding charge/discharge curves. f) dQ/dV curve at 0.5 C. g) Ragone plots of state-of-the-art materials.

which are comparable/superior to most of the recently reported similar materials.[11,16,43,49–55]

The mechanism of sodium storage in the NVP-Mn(0.5) cathode during charging and discharging at 1.4–4.0 V is studied via ex-situ XRD and ex-situ XPS. From **Figure 5**a,b, the diffraction peaks of the material shift, disappear/appear, or split during charging and discharging. Specifically, the (113) and (116) diffraction peaks shift continuously to higher angles during charging to 3.2 V, indicating that $Na^+$ ions are removed and the lattice shrinks. At this stage, the specific electrochemical process is as follows: an electron participates in the reaction ($V^{2+}/V^{3+}$) and $Na_4V_{1.5}Mn_{0.5}(PO_4)_3$ is transformed into $Na_3V_{1.5}Mn_{0.5}(PO_4)_3$. The absence of a new phase and the disappearance of an original phase indicate a typical single-phase reaction mechanism.[16,43] With increasing the voltage from 3.2 to 3.7 V, the crystal faces of (113) and (116) show more obvious high-angle movement than the previous stage, in which 1.75 $Na^+$ ($V^{3+}/V^{4+}$ and $Mn^{2+}/Mn^{3+}$) is removed (i.e., $Na_3V_{1.5}Mn_{0.5}(PO_4)_3$ and is converted to $Na_{1.25}V_{1.5}Mn_{0.5}(PO_4)_3$), and the (104) peak splits into two peaks, while the (300) peak disappears, indicating a typical bi-phase reaction.[27] When further charging to 4.0 V, $V^{4+}$ is transformed into $V^{5+}$, and $Na_{1.25}V_{1.5}Mn_{0.5}(PO_4)_3$ continues to shed 0.25 $Na^+$ to generate $NaV_{1.5}Mn_{0.5}(PO_4)_3$. In contrast with the charging process, the diffraction peaks completely reverse to the initial peak positions when the discharge reaches 1.4 V, indicating that $Na^+$ ions are reversible deintercalation in the NVP-Mn(0.5) with different charge/discharge states. Besides, Figure 5c schematically illustrates the extraction/insertion process of $Na^+$ in the NVP-Mn(0.5). Obviously, the NVP-Mn(0.5) undergoes three $Na^+$ de/intercalation during charging and discharging, and the phase transitions are highly reversible. The cyclic voltammetry (CV) and ex-situ XPS of the NVP-Mn(0.5) during the second charge–discharge cycle are further investigated to explore the conversion of specific redox couples in the electrochemical reaction (Figure 5d–f). The CV measurements are carried out for the NVP-Mn(0)and NVP-Mn(0.5) in 1.4–4.0 V at 0.05 mV $s^{-1}$. The separation degree ($\Delta V$) of the anodic and cathodic peaks for the NVP-Mn(0) and NVP-Mn(0.5) are listed in Table S7 (Supporting Information). Compared with the NVP-Mn(0), the much smaller $\Delta V$ of the NVP-Mn(0.5) indicates that the introduction of $Mn^{3+}$ into the NVP greatly improves the reversibility of the electrochemical reaction.[48] Two pairs of peaks of the NVP-Mn(0) and NVP-Mn(0.5) are located at ≈1.7 and 3.5 V, which are attributed to the common redox couples of $V^{2+}/V^{3+}$ and $V^{3+}/V^{4+}$ (it represents $V^{3+}/V^{4+}$ and $Mn^{2+}/Mn^{3+}$ in the NVP-Mn(0.5)) in the NVP-based cathodes. In addition,

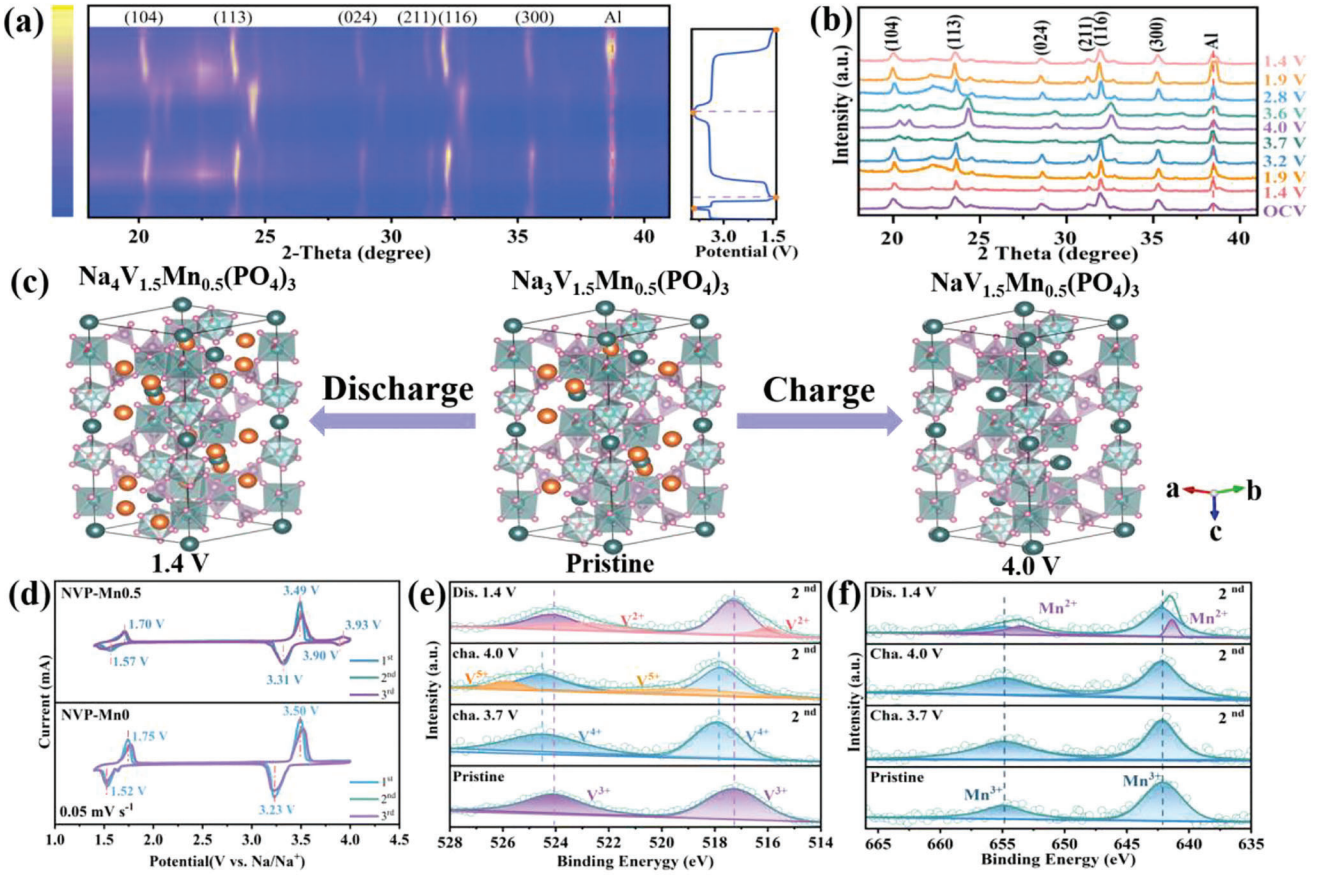


**Figure 5.** a) 2D contour plots of ex-situ XRD patterns of NVP-Mn(0.5) in different charge and discharge states. b) Corresponding XRD patterns of NVP-Mn(0.5) electrodes on some selected materials. c) Schematic illustration of the structural change of NVP-Mn(0.5) electrode on cycling. d) CV curves of NVP-Mn(0.5) and NVP-Mn(0). Ex-situ XPS spectra of: e) V 2p and f) Mn 2p of NVP-Mn(0.5).

the NVP-Mn(0.5) possesses a pair of additional redox couple at 3.9 V ($V^{4+}/V^{5+}$) (Figure 5d), which can be further verified by ex-situ XPS characterization for the NVP-Mn(0.5). The ex-situ XPS spectra of the NVP-Mn(0.5) at different states (pristine, charged (3.7 V), charged (4.0 V), and discharged (1.4 V)) are shown in Figure 5e,f. As shown in Figure 5e, the V element in the initial sample is $V^{3+}$. When charged to 3.7 V, the peak shifts to a higher binding energy and the V exists only as $V^{4+}$, indicating a complete conversion of $V^{3+}$ to $V^{4+}$. When further charging to 4.0 V, $V^{4+}$ and $V^{5+}$ coexist in the material, intuitively revealing that part of $V^{4+}$ is oxidized to form $V^{5+}$.[34,48] From Figure 5f, when discharging to 1.4 V, the coexistence of $Mn^{2+}$ and $Mn^{3+}$ can be found. At 3.7 V, it only exists in the form of trivalent $Mn^{3+}$, suggesting that $Mn^{2+}/Mn^{3+}$ redox couples participate in the electrochemical process, which is consistent with the above analyses.

The kinetic characteristics of the NVP-Mn(0.5) are further studied to reveal the origins of the improved electrochemical properties. The $Na^+$ diffusion coefficients ($D_{Na}$) of the NVP-Mn(0) and the NVP-Mn(0.5) are appraised by Galvanostatic intermittent titration technique (GITT) (**Figure 6**a and Figure S10, Supporting Information). Clearly, the $D_{Na}$ of the NVP-Mn(0.5) is calculated to be $10^{-8}$ to $10^{-10}$ $cm^2$ $s^{-1}$, higher than that of the NVP-Mn(0) ($10^{-8}$ to $10^{-12}$ $cm^2$ $s^{-1}$) and most advanced cathodes. The average $D_{Na}$ of the NVP-Mn(0) and NVP-Mn(0.5) are further calculated to be $1.8793 \times 10^{-9}$ and $1.0839 \times 10^{-8}$, respectively (Table S8, Supporting Information), indicating that the $D_{Na}$ of the NVP-Mn(0.5) is improved by nearly one order of magnitude, which is favorable for the rate performance of the material. The electrochemical impedance spectroscope (EIS) reveals that the NVP-Mn(0.5) has lower charge-transfer resistance ($R_{ct}$) and faster $Na^+$ diffusion coefficient when compared with the NVP-Mn(0) (Figure 6b,c and Table S9, Supporting Information), implying that the NVP-Mn(0.5) has much superior reaction kinetics than the material without the Mn doping. The $R_{ct}$ value (Figure S11, Supporting Information) of the NVP-Mn($x$) is minimized at $x = 0.5$, and thus NVP-Mn(0.5) has the best electrochemical kinetics among four materials. The CV curves of the NVP-Mn(0.5) at various sweep rates are used to understand the capacitance contribution to the total capacity (Figure 6d). As shown in Figure 6e, the b values of the 1–6 peaks are in the range of 0.72–0.98, indicating the coexistence of capacitance and diffusion behaviors in the NVP-Mn(0.5).[16,38] The pseudocapacitance contributions of NVP-Mn(0) and NVP-Mn(0.5) are shown in Figure 6f and Figures S12–S13 (Supporting Information). Obviously, the pseudocapacitive contributions of NVP-Mn(0) and NVP-Mn(0.5) increase with the scan rate (Figure 6f and Figure S13c, Supporting Information). It can be seen that the NVP-Mn(0.5) shows larger pseudocapacitive contributions at all scan rates compared

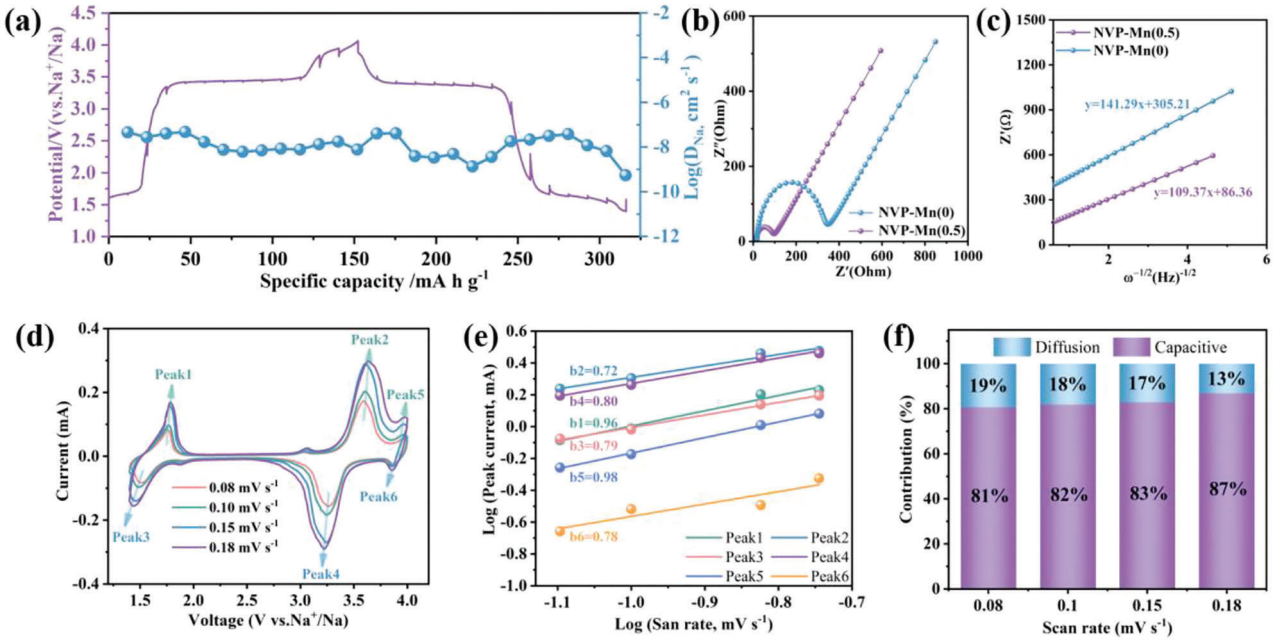


**Figure 6.** Kinetic performance. a) GITT curve and DNa of NVP-Mn(0.5). b) EIS spectra and c) corresponding relationship between Z' and $\omega-1/2$ in the low-frequency region of NVP-Mn(0) and NVP-Mn(0.5). d) CV curves, e) corresponding b-values, and f) pseudocapacitance contribution of NVP-Mn(0.5) at various scan rates.

with the material with $x = 0$, reaching 87% at 0.18 mV $s^{-1}$ for the NVP-Mn(0.5), which is 14% higher than that of NVP-Mn(0) (Figures S12 and S13b, Supporting Information). Thus, the extended lifespan and improved rate properties of NVP-Mn(0.5) may be attributed to nonfaradic processes.

The crystal structures of the NVP-Mn(0) and NVP-Mn(0.5) are simulated in **Figure 7**a and Figure S14 (Supporting Information). To determine the electronic effect on the doping of $Mn^{3+}$ into the NVP, the calculation plots of partial density of state (PDOS) and total density of state (TDOS) of the NVP-Mn(0) and NVP-Mn(0.5)

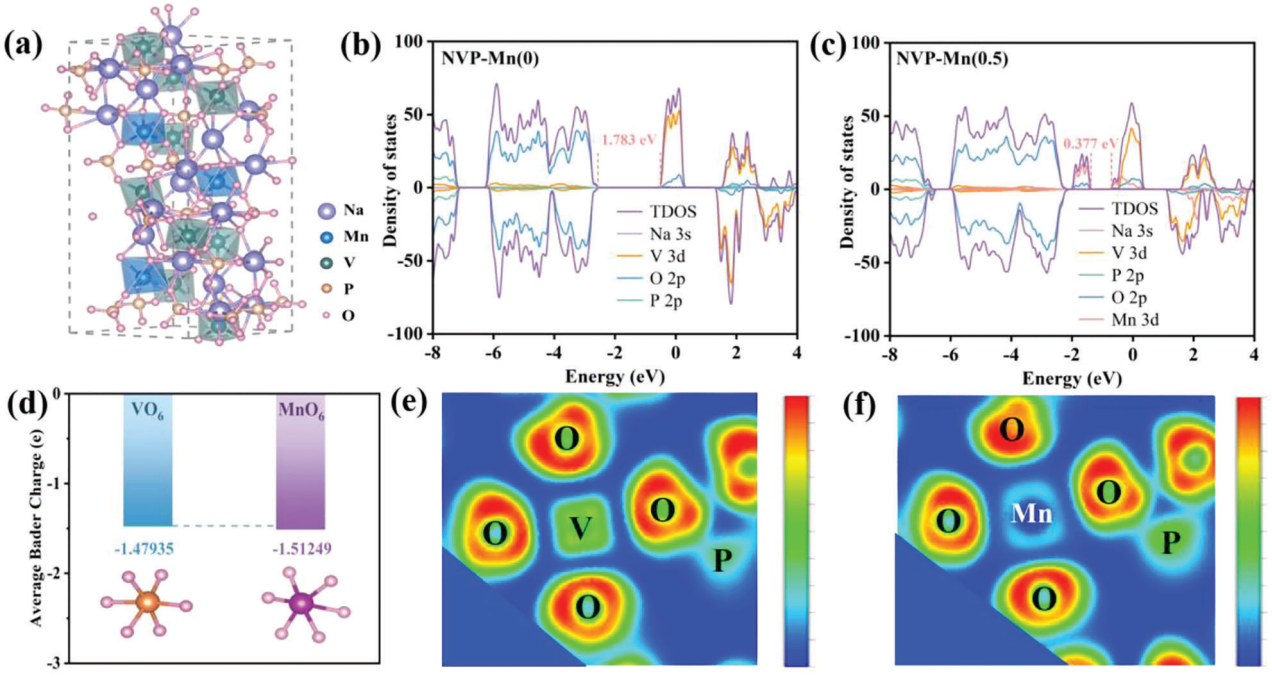


**Figure 7.** a) Structure diagram of NVP-Mn(0.5). DOS and corresponding PDOS diagram of: b) NVP-Mn(0) and c) NVP-Mn(0.5). d) Bader charge of O atoms. ELF maps of: e) NVP-Mn(0) and f) NVP-Mn(0.5).

are displayed in Figure 7b,c. Compared with the NVP-Mn(0), Na 3s, V 3d, P 2p, and O 2p orbitals, as well as additional Mn 3d orbitals, can also be noticed in the NVP-Mn(0.5). Notably, the band gap of the NVP-Mn(0.5) is reduced to 0.377 eV due to the hybridized Mn 3d orbitals, which is much smaller than that of NVP-Mn(0) (1.783 eV), demonstrating that the doping of $Mn^{3+}$ causes an enhancement of electron density and $Na^+$ charge-transfer ability,[23,27] thus contributing to the decent electronic conductivity of the NVP-Mn(0.5). The lower band gap of the NVP-Mn(0.5) may be attributed to the fact that Mn ($[Ar]3d^5 4s^2$) has two more unpaired valence electrons than V($[Ar]3d^3 s^2$), which may also be an intrinsic reason for the high potential $V^{5+}/V^{4+}$ activated in the NVP-Mn(0.5).[11] The effects of $Mn^{3+}$ doping on the structure of NVP-Mn($x$) are analyzed using Bader charge, and the result is shown in Figure 7d. From Figure 7d, the average charge of O in the $MnO_6$ of NVP-Mn(0.5) is much negative than that in the $VO_6$ of NVP-Mn(0), which indicates that the substitution of $Mn^{3+}$ for $V^{3+}$ enhances the structural stability of NASICON framework, being conducive to a long-term stable cycle. In addition, stronger P–O bonds can be observed in the Electron Localization Function (ELF, Figure 7e,f), which is consistent with the Bader charge results. These results strongly suggest that the substitution of $Mn^{3+}$ for $V^{3+}$ enhances the framework stability and facilitates the realization of the long-term stable cycle.

## 3. Conclusion

In summary, the $Na_3V_{2-x}Mn_x(PO_4)_3$ has been designed by introducing low-cost and environmentally friendly $Mn^{3+}$ into NASICON-type $Na_3V_2(PO_4)_3$. After the addition of $Mn^{3+}$, the band gap is significantly reduced by 1.406 eV and thus the electronic conductivity is greatly enhanced. The redox couple of $V^{4+}/V^{5+}$ is successfully activated at 3.9 V, leading to a reversible three-electron reaction; and the doping of $Mn^{3+}$ results in nanosized and uniform particles. Consequently, the $Na_3V_{1.5}Mn_{0.5}(PO_4)_3$ cathode exhibits a high reversible discharge capacity of 170.9 mAh $g^{-1}$ at 0.5 C with an ultrahigh energy density of 577 Wh $kg^{-1}$. What is more, the sodium-storage mechanism for Mn-doped $Na_3V_2(PO_4)_3$ consists of both single-phase and bi-phase reactions. The unpaired electrons of Mn on 3d may be the key to successfully trigger the $V^{4+}/V^{5+}$ couple and activate the reversible three-electron reaction in the NVP-based material. The present work develops a feasible strategy to develop high-energy density cathodes for sodium-ion batteries by activating the high-potential $V^{4+}/V^{5+}$ redox couple.

## Supporting Information

Supporting Information is available from the Wiley Online Library or from the author.

## Acknowledgements

This work was supported by the Natural Science Foundation of Sichuan Province (grant No. 2022NSFSC0222) and the Sichuan Science and Technology Program (grant No. 2023NSFSC0439).

## Conflict of Interest

The authors declare no conflict of interest.

## Data Availability Statement

The data that support the findings of this study are available from the corresponding author upon reasonable request.

## Keywords

high-energy density, $Mn^{3+}$ doping, $Na_3V_2(PO_4)_3$, sodium-ion batteries, three-electron effect

Received: May 12, 2023
Revised: August 9, 2023
Published online: August 24, 2023

[1] W. Yu, Y. Guo, S. Xu, Y. Yang, Y. Zhao, J. Zhang, *Energy Storage Mater.* **2022**, *54*, 172.
[2] Y. Fan, Y. Kong, P. Jiang, G. Zhang, J. Cong, X. Shi, Y. Liu, P. Zhang, R. Zhang, Y. Huang, *Chem. Eng. J.* **2023**, *463*, 142278.
[3] K. Chayambuka, G. Mulder, D. L. Danilov, P. H. Notten, *Adv. Energy Mater.* **2020**, *10*, 2001310.
[4] J. Zhang, Y. Lei, Z. Lin, P. Xie, H. Lu, J. Xu, *Chem. Eng. J.* **2022**, *436*, 135011.
[5] J. Sun, X. Li, Y. Huang, G. Luo, D. Tao, J. Yu, L. Chen, Y. Chao, W. Zhu, *Chem. Eng. J.* **2023**, *453*, 139485.
[6] W. Li, J. Li, R. Li, X. Li, J. Gao, S. M. Hao, W. Zhou, *Battery Energy* **2022**, *2*, 20220042.
[7] Y. Liu, C. Sun, Y. Li, H. Jin, Y. Zhao, *Energy Storage Mater.* **2023**, *57*, 69.
[8] R. Deng, Q. Li, P. Wang, Q. Zheng, Y. Huo, F. Xie, D. Lin, *Electrochim. Acta* **2022**, *432*, 141157.
[9] L. Fang, N. Bahlawane, W. Sun, H. Pan, B. B. Xu, M. Yan, Y. Jiang, *Small* **2021**, *17*, 2101137.
[10] Q. Li, R. Deng, Y. Chen, J. Gong, P. Wang, Q. Zheng, Y. Huo, F. Xie, X. Wei, C. Yang, D. Lin, *Small* **2023**, *19*, 2303642.
[11] M. Chen, W. Hua, J. Xiao, J. Zhang, V. W.-h. Lau, M. Park, G.-H. Lee, S. Lee, W. Wang, J. Peng, *J. Am. Chem. Soc.* **2021**, *143*, 18091.
[12] C. Tao, O. Baixue, F. Xiaowen, Z. Weili, L. Weifang, L. Kaiyu, *Carbon Energy* **2022**, *4*, 170.
[13] H.-R. Yao, W.-J. Lv, X.-G. Yuan, Y.-J. Guo, L. Zheng, X.-A. Yang, J. Li, Y. Huang, Z. Huang, P.-F. Wang, *Nano Energy* **2022**, *97*, 107207.
[14] M. Arianna, M. G. A. B., P. P. Paolo, G. Claudio, P. Michele, *ACS Energy Lett.* **2021**, *6*, 2470.
[15] Z. Lu-Lu, C. Zhao-Yao, F. Xin-Yuan, Y. Bo, T. Hua-Chao, Y. Xue-Lin, *Chem. Eng. J.* **2022**, *433*, 133739.
[16] W. Zhang, Y. Wu, Z. Xu, H. Li, M. Xu, J. Li, Y. Dai, W. Zong, R. Chen, L. He, *Adv. Energy Mater.* **2022**, *12*, 2201065.
[17] Z. Y. Gu, J. Z. Guo, J. M. Cao, X. T. Wang, X. X. Zhao, X. Y. Zheng, W. H. Li, Z. H. Sun, H. J. Liang, X. L. Wu, *Adv. Mater.* **2022**, *34*, 2110108.
[18] T. Liu, B. Wang, X. Gu, L. Wang, M. Ling, G. Liu, D. Wang, S. Zhang, *Nano Energy* **2016**, *30*, 756.
[19] Q. Zhou, L. Wang, W. Li, K. Zhao, M. Liu, Q. Wu, Y. Yang, G. He, I. P. Parkin, P. R. Shearing, *Electrochem. Energy Rev.* **2021**, *4*, 793.
[20] Y. Zhao, X. Gao, H. Gao, H. Jin, J. B. Goodenough, *Adv. Funct. Mater.* **2020**, *30*, 1908680.
[21] C. Shuangqiang, W. Chao, S. Laifa, Z. Changbao, H. Yuanye, X. Kai, M. Joachim, Y. Yan, *Adv. Mater.* **2017**, *29*, 1700431.
[22] J. Li, Y. Chen, S. He, Y. Yang, Y. Wang, L. Guo, *Chem. Eng. J.* **2023**, *452*, 139311.
[23] X. Liu, J. Gong, X. Wei, L. Ni, H. Chen, Q. Zheng, C. Xu, D. Lin, *J. Colloid. Interface Sci.* **2022**, *606*, 1897.
[24] L. Shen, Y. Li, C. Hu, Z. Huang, B. Wang, Y. Wang, Q. Liu, F. Ye, *Mater. Today Chem.* **2023**, *30*, 101506.

[25] C. Xu, J. Zhao, E. Wang, X. Liu, X. Shen, X. Rong, Q. Zheng, G. Ren, N. Zhang, X. Liu, X. Guo, C. Yang, H. Liu, B. Zhong, Y. S. Hu, *Adv. Energy Mater.* **2021**, *11*, 2100729.
[26] T. Or, S. W. D. Gourley, K. Kaliyappan, Y. Zheng, M. Li, Z. Chen, *Electrochem. Energy Rev.* **2022**, *5*, 20.
[27] C. Sun, Y. Zhao, Q. Ni, Z. Sun, X. Yuan, J. Li, H. Jin, *Energy Storage Mater.* **2022**, *49*, 291.
[28] X. Liu, G. Feng, Z. Wu, Z. Yang, S. Yang, X. Guo, S. Zhang, X. Xu, B. Zhong, Y. Yamauchi, *Chem. Eng. J.* **2020**, *386*, 123953.
[29] C. Yanjun, C. Jun, W. Chao, H. Zhenfeng, W. Yanzhong, L. Dan, G. Li, *Chem. Eng. J.* **2020**, *413*, 127451.
[30] L. Liang, X. Li, F. Zhao, J. Zhang, Y. Liu, L. Hou, C. Yuan, *Adv. Energy Mater.* **2021**, *11*, 2100287.
[31] M. Li, C. Sun, Q. Ni, Z. Sun, Y. Liu, Y. Li, L. Li, H. Jin, Y. Zhao, *Adv. Energy Mater.* **2023**, *13*, 2203971.
[32] C. Xu, R. Xiao, J. Zhao, F. Ding, Y. Yang, X. Rong, X. Guo, C. Yang, H. Liu, B. Zhong, *ACS Energy Lett.* **2021**, *7*, 97.
[33] Z. Wang, G. Cui, Q. Zheng, X. Ren, Q. Yang, S. Yuan, X. Bao, C. Shu, Y. Zhang, L. Li, *Small* **2023**, *19*, 2206987.
[34] J. Lee, S. Park, Y. Park, J. Song, B. Sambandam, V. Mathew, J.-Y. Hwang, J. Kim, *Chem. Eng. J.* **2021**, *422*, 130052.
[35] S. Ghosh, N. Barman, M. Mazumder, S. K. Pati, G. Rousse, P. Senguttuvan, *Adv. Energy Mater.* **2020**, *10*, 1902918.
[36] M. Su, J. Shi, Q. Kang, D. Lai, Q. Lu, F. Gao, *Chem. Eng. J.* **2022**, *432*, 134289.
[37] Q. Ni, Y. Bai, F. Wu, C. Wu, *Adv. Sci.* **2017**, *4*, 1600275.
[38] W. Zhang, Z. Xu, H. Li, M. Xu, S. Wang, Z. Li, A. Wang, L. Zhang, L. He, S. Li, *Chem. Eng. J.* **2022**, *433*, 133542.
[39] M. Hadouchi, N. Yaqoob, P. Kaghazchi, M. Tang, J. Liu, P. Sang, Y. Fu, Y. Huang, J. Ma, *Energy Storage Mater.* **2021**, *35*, 192.
[40] V. Soundharrajan, S. Nithiananth, K. Sakthiabirami, J. H. Kim, C.-Y. Su, J.-K. Chang, *J. Mater. Chem. A* **2022**, *10*, 1022.
[41] R. Klee, P. Lavela, M. Aragón, R. Alcántara, J. Tirado, *J. Power Sources* **2016**, *313*, 73.
[42] J. Zhang, X. Zhao, Y. Song, Q. Li, Y. Liu, J. Chen, X. Xing, *Energy Storage Mater.* **2019**, *23*, 25.
[43] C. Xu, J. Zhao, E. Wang, X. Liu, X. Shen, X. Rong, Q. Zheng, G. Ren, N. Zhang, X. Liu, *Adv. Energy Mater.* **2021**, *11*, 2100729.
[44] C. Xu, J. Zhao, Y. A. Wang, W. Hua, Q. Fu, X. Liang, X. Rong, Q. Zhang, X. Guo, C. Yang, *Adv. Energy Mater.* **2022**, *12*, 2200966.
[45] X. Yue, Y. Dong, J. Gong, Y. Gao, K. H. Lam, Q. Zheng, D. Lin, *J. Alloys Compd.* **2023**, *947*, 169591.
[46] Y. Zhou, S. Guo, S. Li, Y. Ling, W. Ren, H. Zhou, L. Wang, X. Cao, S. Liang, *J. Power Sources* **2022**, *521*, 230974.
[47] C. Xu, J. Zhao, E. Wang, X. Liu, X. Shen, X. Rong, Q. Zheng, G. Ren, N. Zhang, X. Liu, *Adv. Energy Mater.* **2021**, *11*, 2100729.
[48] Y. Liu, C. Sun, Q. Ni, Z. Sun, M. Li, S. Ma, H. Jin, Y. Zhao, *Energy Storage Mater.* **2022**, *53*, 881.
[49] J. Liu, K. Lin, Y. Zhao, Y. Zhou, X. Hou, X. Liu, H. Lou, K.-h. Lam, F. Chen, *J. Mater. Chem. A* **2021**, *9*, 10437.
[50] M. Hadouchi, N. Yaqoob, P. Kaghazchi, M. Tang, J. Liu, P. Sang, Y. Fu, Y. Huang, J. Ma, *Energy Storage Mater.* **2021**, *35*, 192.
[51] W. Zhou, L. Xue, X. Lü, H. Gao, Y. Li, S. Xin, G. Fu, Z. Cui, Y. Zhu, J. B. Goodenough, *Nano Lett.* **2016**, *16*, 7836.
[52] Y. Fang, Q. Liu, L. Xiao, X. Ai, H. Yang, Y. Cao, *ACS Appl. Mater. Interfaces* **2015**, *7*, 17977.
[53] J. Yang, H. Wang, P. Hu, J. Qi, L. Guo, L. Wang, *Small* **2015**, *11*, 3744.
[54] H. Kim, R. Shakoor, C. Park, S. Y. Lim, J. S. Kim, Y. N. Jo, W. Cho, K. Miyasaka, R. Kahraman, Y. Jung, *Adv. Funct. Mater.* **2013**, *23*, 1147.
[55] Y. Liu, Y. Xu, X. Han, C. Pellegrinelli, Y. Zhu, H. Zhu, J. Wan, A. C. Chung, O. Vaaland, C. Wang, *Nano Lett.* **2012**, *12*, 5664.